Ligand-mode directed selectivity in Cu–Ag core–shell based gas diffusion electrodes for CO_2 electroreduction

Ligand-Mode Directed Selectivity in Cu-Ag Core-Shell based Gas Diffusion Electrodes for CO_2 Electroreduction

Erdem Irtem[*1], *Daniel Arenas Esteban*[2], *Miguel Duarte*[1], *Daniel Choukroun*[1], *Seungho Lee*[3], *Maria Ibáñez*[3], *Sara Bals*[2] *and Tom Breugelmans**[1, 4]

[1]*Research Group Applied Electrochemistry & Catalysis (ELCAT), University of Antwerp, Universiteitsplein 1, 2610, Wilrijk, Belgium,* [2]*Electron Microscopy for Materials Science (EMAT), Department of Physics, University of Antwerp, Groenenborgerlaan 171, 2020 Antwerp* [3]*Institute of Science and Technology (IST) Austria, Am Campus 1, A-3400 Klosterneuburg, Austria, Belgium,* [4]*Separation & Conversion Technologies, VITO, Boeretang 200, 2400 Mol, Belgium*

keywords: core-shell, ligand effect, CO2 electroreduction, gas diffusion electrode, triple phase boundary, electrical conductivity

Abstract

Bimetallic nanoparticles with tailored size and specific composition have shown promise as stable and selective catalysts for electrochemical reduction of CO_2 (CO2R) in batch-systems. Yet, limited effort was devoted to understand the effect of ligand coverage and post-synthesis treatments on CO_2 reduction, especially under industrially applicable conditions, such as at high currents (>100 mA/cm^2) using gas diffusion electrodes (GDE) and flow reactors. In this work, Cu-Ag core-shell nanoparticles (11 ± 2 nm) were prepared with three different surface modes; (i) capped with oleylamine, (ii) capped with isopropylamine and (iii) surfactant-free with a reducing borohydride agent; Cu−Ag (OAm), Cu−Ag (MIPA) and Cu−Ag ($NaBH_4$), respectively. The ligand exchange and removal was evidenced by infrared spectroscopy (ATR-FTIR) analysis, whereas high-resolution scanning transmission electron microscopy (HAADF-STEM) showed their effect on the interparticle distance and nanoparticle rearrangement. Later on, we developed a process-on-substrate method to track these effects on CO2R. Cu-Ag (OAm) gave a lower on-set potential for hydrocarbon production whereas Cu−Ag (MIPA) and Cu−Ag ($NaBH_4$) promoted syngas production. The electrochemical impedance and surface area analysis on the well-controlled electrodes showed gradually increase in the electrical conductivity and the active surface area after each surface treatment. We found that the increasing amount of the triple phase boundaries (the meeting point for the electron – electrolyte – CO_2 reactant) affects the required electrode potential and eventually C_{+2e^-}/C_{2e^-} product ratio. This study highlights the importance of the electron transfer to those active sites affected by the capping agents – particularly on larger substrates that are crucial for their industrial application.

INTRODUCTION

The electrochemical conversion of CO_2 (CO2R) to value added products using renewable electricity is an attractive pathway to close the carbon cycle that causes severe environmental issues[1]. Much attention has been devoted to increase CO2R reaction rate and product selectivity for its commercial valorization[2]. Herein, the bimetallic core-shell nanoparticles (c/s NPs) appeal as electrocatalysts since a sensitive metal at the core can be protected with a small amount of precious metal shell to remain stable under demanding conditions, such as high current densities. Most studies involving c/s NPs showed high faradaic efficiency and activity such as, Cu@In_2O_3 (67 % CO at 8 mA/cm^2) [3], Ag@Cu (82 % CO at 3.1 mA/cm^2) [4], Cu@SnO (93 % CO at 4.6 mA/cm^2) [5], $AuCu_3$@Au (97% CO at 5.4 mA/cm^2) [6] and AuFe@Au (97 % CO at 11.3 mA/cm^2) [7]. The underlying drivers of the catalytic activity were linked to different mechanisms such as a strain effect, surface defects or alloy interfaces[8], but the effect of the capping ligand on electrochemical CO2R was often disregarded. For instance, the ligands from the synthesis were found to block 1/4th of the AuCu@Au NPs electrochemically active surface area (ECSA) detected by the underpotential deposition[9]. Yet, the change of selectivity in terms of faradaic efficiency (61% H_2 to 80% CO) was assigned to atomic ordering, neglecting the different type of ligands used to synthesize them (e.g. oleic acid vs. oleylamine). Recently, Buckley et. al. studied oxide derived Cu (Cu-OD) catalysts that are modified with protic or aprotic functional groups. The authors suggested a relationship between hydrophobicity and product selectivity (CO vs. HCOOH) pointing to the H^+/H_2O availability at the metal-ligand interface of the Cu surface[10]. In another study[11] 25 nm Ag-Cu nanodimers, synthesized with an hexadecylamine ligand showed a good performance for CO2R, but the possible influence of the ligand on the CO2R activity was not investigated. A follow-up study[12] confirmed the influence of ligand treatment by showing the

change in CO2R activity of Ag-NPs towards CO using different lengths of hydrocarbon tail in imidazolium-based ligands[11]. Nevertheless, both studies were conducted on flat glassy carbon electrodes (~0.2 cm^2 geometric surface area) and in H-type batch cells, where mass transfer limitations may change the local pH near the electrode – influencing the catalytic performance – at high current density[2]. Given the meticulous efforts to design and control the atoms and molecules at the nanoscale, it is equally important to investigate their intrinsic activity and selectivity under industrially relevant conditions[13]. The ligands employed during colloidal synthesis may influence the environment of the active sites for CO2R, because they limit not only physical but also electrical contact; in-between the individual particles and also with the substrate. A previous study[14] on the Cu-Ag conductive films showed that the resistivity of the oleylamine-capped nanoparticles after annealing at 250 ºC for 60 min was as high as ~100 Ω·cm. The resistance drastically decreased after annealing at higher temperatures with a cost of nanoparticle aggregation. In one hand, the annealing would decrease the number of active sites for the electrocatalysis, on the other hand the resistance created by the ligands would lead to a large ohmic drop across the electrode especially at high currents. Hence, the true industrial potential of c/s NPs must be evaluated at elevated current densities (> 100 mA/cm^2) where the active sites, i.e. triple phase boundaries (TPBs), where CO_2 gas continuously unite with the electrons of the catalyst electrode and the ions from the electrolyte.

Here, we therefore applied a process on substrate (or solid-state ligand exchange) method for the exchange or removal of the oleylamine ligand capped on the Cu-Ag nanoparticle coated GDEs. The catalyst electrodes were tested before and after each treatment to explore their effect on CO2R performance in a flow-cell. Ligand replacement and its removal were verified with ATR-FTIR analysis. The morphological (intra- and inter particle) changes of the nanoparticles

were analyzed using high-resolution HAADF-STEM. Further electrochemical techniques such as electrochemical impedance spectroscopy (EIS) and surface area analysis (ECSA) were conducted on the well-defined surface of the glassy carbon electrodes. Metal-ligand interactions were found to be essential for nanoparticle stability, but additional electrochemical analysis also showed their effect on TPBs and consequently on the electroreduction of CO_2. The surface engineering methods discussed here, such as the ligand exchange reactions, would be critical for the use of controlled-nanoparticles in the upscaling of CO_2 conversion systems.

EXPERIMENTAL SECTION

Materials: Copper(II) formate tetrahydrate ($(HCO_2)_2Cu•4H_2O$, Alfa Aesar 98%), silver nitrate ($AgNO_3$, Alfa Aesar 99+%), Oleylamine (OAm), Paraffin, MIPA, NaOH, NaBH4 water (Milli-Q, 18.2 MΩ), hexane (Sigma-Aldrich, mixture of isomers, anhydrous, ≥99%), ethanol (Sigma-Aldrich, pure, anhydrous, ≥99.5%), isopropanol (Sigma-Aldrich, anhydrous, 99.5%), Perfluorosulfonic acid-PTFE copolymer (5% w/w solution, Alfa Aesar). Nafion 117 membrane, dimensionally stable anode (SKU: 592777) and gas diffusion electrode Sigracet 39 BC GDL (GDE) were purchased from Fuel Cell store (USA). Copper nanopowder (25 nm particle size) and silver nanospheres (100 nm average particle size) particles were purchased from Sigma Aldrich for comparison with commercial metal catalysts. All materials were used without further purification except cupric (II) formate which was kept under vacuum in a container with silica beads at 90°C overnight.

*Synthesis of Cu-Ag core-shell nanoparticles: T*wo-step colloidal synthesis method was performed using a three neck flask and Schlenk line techniques according to a literature procedure[15]. Briefly, in the first step, copper formate tetrahydrate (240 mg) and oleylamine (2.3

mL) were dissolved in paraffin (16 mL) at 70°C under vacuum for 30 minutes. Then, the solution was heated up to 170 °C and held for 30 min under constant stirring at 500 rpm and bubbling of Argon gas. Immediately after, the solution (with a ruby-red color) was cooled down with an ice-bath to slow down the growth of the copper nanoparticles. The silver shell was formed in the second step by dissolving silver nitrate (57.6 mg) with oleylamine (7 mL) in separate flask under inert atmosphere and transferred to the copper solution without exposing to air using a cannula setup. This was followed by heating the mixture up to 80 °C and hold for 2 hours under constant stirring at 500 rpm and bubbling of Argon gas. After rapid cooling of the mixture, the colloidal particles were precipitated by addition of a Isopropanol:Hexane mixture (1.5x volume of paraffin) and centrifuged at 7500 rpm for 20 minutes. Particles were re-dispersed in hexane and centrifugation – re-dispersion procedure was repeated for two more times.

Catalyst ink and electrode preparation: After colloidal synthesis and cleaning, the concentration of Cu-Ag (7.8 mg/mL) suspension was determined by ICP-MS analysis prior to ink preparation. Accordingly, 10 mg of Cu-Ag (OAm) catalyst nanoparticles were mixed with 2 mL of Isopropanol:Hexane with 1:1 ratio and left to stir for 10 minutes followed by 20 minutes sonication. Later on, 21.5 μL of perfluorosulfonic acid-PTFE copolymer (5% w/w solution) ionomer was added and sonicated for extra 10 minutes. The catalyst ink was coated by spraying with Argon gas onto the GDE substrates fixated on a custom-made vacuum plate (Figure S7) that limits the effective spraying area to 14 cm^2. Sigracet 39-BC gas diffusion electrodes were weighed before and after the spraying to obtain a loading of 0.7 ± 0.05 mg catalyst per cm^2 of the geometric surface area. For comparison, commercial Cu (25 nm) and Ag (100 nm) nanoparticles

were used to prepare similar catalyst inks with 0.7 ± 0.05 mg Cu (or Ag) metal loading per cm^2, as described in the protocol above.

Ligand exchange and removal: For ligand exchange, Cu@Ag (OAm) catalyst loaded GDEs were left for 5 min in methanol solution with 10 % monoisopropylamine (MIPA). Next, the electrodes were rinsed with methanol solution and dried under N_2 stream (Cu@Ag – MIPA). For ligand removal, those electrodes were then immersed in 10 mM NaOH solution with 2 wt. % $NaBH_4$ to detach the capping agents (ligands) from the nanoparticle surface (Cu@Ag – $NaBH_4$).

Physical and chemical characterization: The colloidal suspension of Cu-Ag (OAm) was diluted with hexane and drop-casted onto transmission electron microscopy (TEM) grids. Similar to GDE pre-treatments were conducted on the grids prior to their analysis (ligand exchange, MIPA and reduction with $NaBH_4$). A Thermo Fischer Scientific TITAN electron microscope in the scanning TEM (STEM) mode was employed together with a high-angle annular dark-field (HAADF) detector at 300 kV. Scanning electron microscope (SEM) images of the catalyst loaded GDEs were obtained using a Quanta 250 FEG-SEM at a potential of 5kV with 3.5 spot size. Ultraviolet–visible spectroscopy (UV–Vis) measurements were performed on a Thermo Nicolet Evolution 500 spectrometer with a Xenon lamp coupled with liquid phase accessory in transmission mode suitable for quartz cuvettes. Colloidal inks were diluted with hexane (x250) and spectra were collected against pure hexane solvent between 300 – 800 nm range at a scan speed of 400 nm/min. Infrared spectra of the samples of oleylamine and monoisopropylamine were measured with a Jasco 660 plus FT-IR spectrometer, between 4000 and 350 cm^{-1}, using the KBr pellet method. 300 µL of the pure compound (15 mg/mL) was mixed with dry KBr (400 mg) which was dried in a muffle furnace at 200 °C and used as the white reference. Infrared spectra of the catalyst film coated GDEs were performed using a Bruker Alpha II FT-IR

spectrophotometer with an attenuated total reflectance (ATR) diamond crystal module. Each measurement was an average of 16 scans over a range of 400 – 4000 cm^{-1}. Inductively coupled plasma mass spectrometry (ICP-MS Agilent 7500) was used to determine the concentration of colloidal suspensions and catalyst amount of GDEs. Copper and silver standards were used (Alfa Aesar, Ward Hill, USA) in the same range as the test samples by digesting and diluting with 1% HNO_3 (Fluka TraceSelect, Morris Planes, USA) prior to their analysis.

Electrochemical Measurements and Product Analysis: CO_2 electroreduction (CO_2R) reaction experiments were carried out using a commercial filter-press continuous-flow electrolyzer (ElectroCell Micro Flow Cell®) described elsewhere[16-17]. Briefly, Cu@Ag coated GDE (10.2 cm^2, as cathode) was mounted on a Titanium current collector with specific apertures to permit CO_2 gas flow at its rear side and electrolyte circulation at GDE's catalyst side, facing a leak free Ag/AgCl reference electrode (Innovative Instruments, Inc.). An ion exchange membrane (Nafion® 117, FuelCell Store) was used to divide the cell into two compartments to inhibit product mixture. A dimensionally stable anode (Pt/Ti) was used as the counter electrode for oxygen evolution reaction (OER). Viton gaskets and custom-design PMMA spacers were placed in between to ensure an air-tight assembly and flow promotion, respectively. The catholyte (0.5 M $KHCO_3$) and anolyte (2 M KOH) were circulated using an Ismatec Reglo ICC peristaltic pump at a flow rate of 20 mL/min. Pre-humidified CO_2 were fed by a mass flow controller (Brooks Inst. GF040 Digital TMF Controller/Meter) at 40 mL/min flow rate. The gas samples were analyzed with an in-line Shimadzu 2014 series gas chromatographer equipped with a TCD detector and a micropacked column (Restek Shincarbon ST, 2 m length, 1 mm internal diameter, 100/120 mesh). The initial oven temperature was set at 40 °C. After maintaining it for 3 minutes it was ramped up to 250 °C at 40 °C/min, at which point it was sustained for 3 minutes. The

TCD detector was kept at 280 °C and helium was used as carrier gas at a flow rate of 10 mL/min. A high-performance liquid chromatography (HPLC, Alliance 2695, Waters, USA) combined with a packed column (IC-Pak, Waters, USA) and a PDA detector (2996, Waters, at 210 nm) was employed to detect the formate concentration in the catholyte. A perchloric acid solution (0.1%) was used as the eluent for the HPLC. Our HPLC protocol was able to reach a detection limit as low as ±5 ppm and the error on the presented FE data was lower than 2.7%. Formate was the only quantifiable product detected in the liquid phase. The remaining products were either formed at low concentrations or not any, for the reason that they were not the major products under the employed conditions in this study.

The potential was controlled with a multichannel Autolab potentiostat M204 equipped with an FRA module and a 10 A booster. The ohmic drop between the working and reference electrode were average to 0.55 ohm, from the impedance measurement conducted at every 7 minutes during the experiments at a frequency of 10 kHz. All electrochemical tests were operated and equipment were calibrated at room temperature and pressure, 293.15 K and 760 Torr respectively.

RESULTS & DISCUSSION

Synthesis of Cu-Ag core-shell nanoparticles was conducted in a two-step process as illustrated in Figure 1a. In the first step, the copper nanoparticles (Cu-NPs) were synthesized through thermal decomposition of copper formate in oleylamine and paraffin solution under inert atmosphere. The formate decomposes to give carbon dioxide and hydrogen gas close to 98 °C indicating the on-set of nucleation, which was observed by the rapid change in solution color

from light blue to reddish brown. The temperature was held constant during 30 minutes for the growth of the copper nanoparticles (Cu-NPs). Previous studies showed that after a certain time, the particles do not grow further but rather dissolve and redeposit due to the Ostwald ripening[18]. Thus, the synthesis flask was immediately immersed in an ice bath to stop the reaction and to ensure a uniform Cu-NPs size. The aliquots taken at this step were analyzed by HAADF-STEM. Figure S1 shows the single crystal Cu-NPs which exhibited spherical shape with an average particle size of around ~11 nm in accordance with the previous results[19] with OAm:Cu-formate (4:1) ratio. In the second step, the Ag shell was formed around Cu-NPs by the galvanic replacement reaction, which took place at 80 °C for 2 hours. A mild temperature was necessary to complete Ag shell formation, since galvanic exchange at room temperature results in a thin or incomplete shell formation leading to Ag dewetting and copper oxidation over time[20]. Higher temperatures (> 110 °C) trigger self-nucleation of silver and must be avoided. The aliquots were taken at different intervals of the second step (2^{nd}, 30^{th}, 60^{th} and 120^{th} min) to investigate the shell formation by UV-visible spectroscopy (Figure 1b).

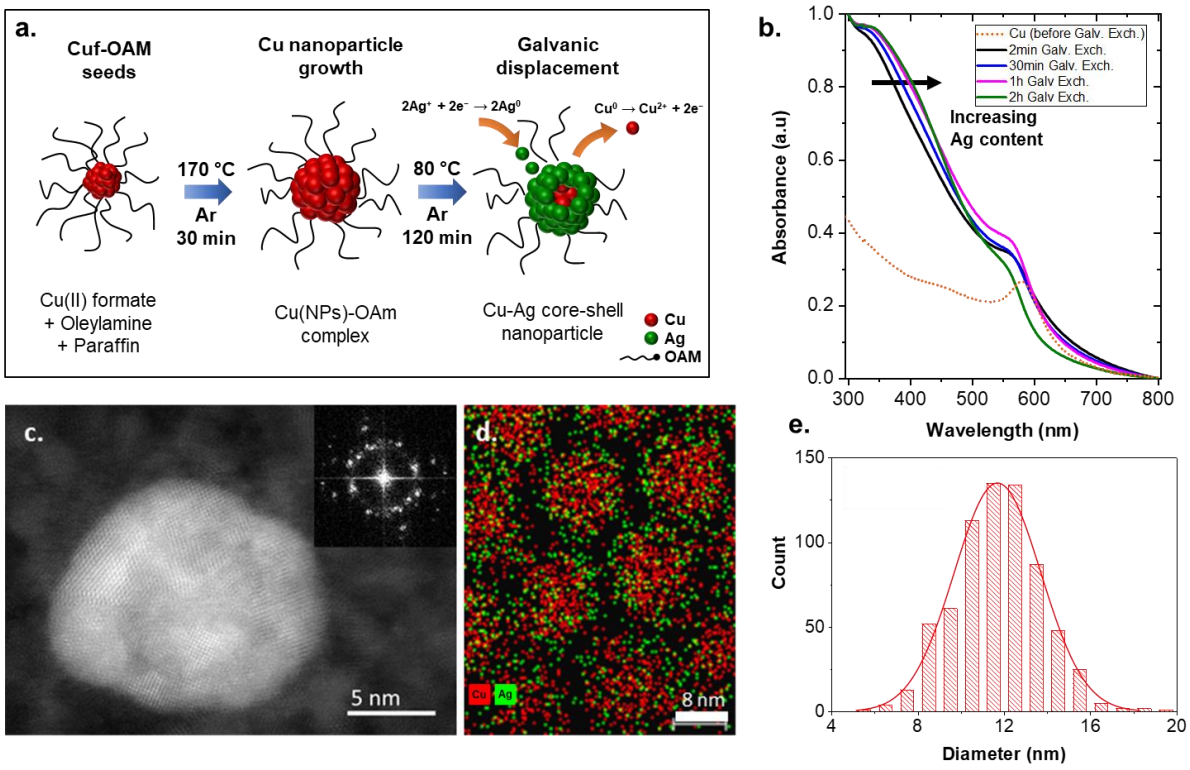

Figure 1. (a) Schematic illustration of the two-step colloidal synthesis of Cu-Ag core-shell nanoparticles; **(b)** Optical extinction spectra of core-shell Cu@Ag nanoparticles from aliquots taken during galvanic exchange– plots are normalized to the maximum peak **(c)** High resolution HAADF-STEM image of a single core-shell like Cu-Ag bimetallic nanoparticle (inset image is the Fast Fourier Transform (FFT) of the image where the quasi ring formed shows the different crystals domains present) **(d)** Energy dispersive X-ray spectroscopy (EDX) analysis of several nanoparticles showing the elemental distribution **(e)** Particle size distribution.

The localized surface plasmon resonance (LPSR) of Ag around λ = 400 nm formed a noticeable shoulder as the reaction proceeds. The colloidal dispersion also shows a broad band at λ = 585 nm corresponding to the LSPR of Cu, which shifts to lower wavelengths compared to

the resonance from Cu-NPs (Figure 1b). These findings are in good agreement with the results reported by Alivisatos et. al.[21] who found similar redshifts towards the standard Ag absorption. Also, the absence of infrared absorption of Cu_2O (≥700 nm) justifies the oxide free form of the core-shell. HR-STEM analysis was performed to investigate the particle morphology. The contrast difference in Figure 1c can be observed on the particle images that originate from the two main factors. First, the Ag shell is not monocrystalline as several domains can be found. Moreover, the selected area diffraction (SAED) analysis (Figure 1c inset image) exposed the presence of quasi-rings in the digital diffraction pattern, again suggesting a polycrystalline structure inducing diffraction contrast in the image. Secondly, the lower atomic number of copper against silver in the center of the nanoparticle gives it a hollow appearance, but after EDX analysis shown in Figure 1d, it can be ensured that the Cu is located inside the core of the particles. These microscopic and spectroscopic results evidenced a core-shell morphology where the copper core was surrounded by a silver shell with a spherical morphology and an average particle size of 11.7 ± 2 nm (See Supporting Info† at Figure S2 for their TEM images at different magnifications).

The common protocol for surfactant or ligand removal[7] from as-synthesized NPs is annealing at temperatures above 150°C . As introduced in the earlier section, soft treatment may leave residues that alter the active sites, whereas the harsher conditions change the particle shape entirely due to the sintering effect[22]. Yet another alternative is ligand exchange and removal by a solvent-assisted wet chemistry method which has shown to improve the electrical conductivity[23]. The steps of this protocol were recorded with digital pictures and given in Figure S3. The biphasic mixtures in the pictures show the change in their appearance as a result of a change of their surface groups. Figure S3a shows that oleylamine-stabilized particles, referred as Cu-Ag

(OAm), were well-dispersed in hexane thanks to the steric stabilization of the long chain ligand. In Figure S3b, monoisopropylamine (MIPA, a weak base) was used for the ligand exchange due to its pK_a of 10.6; as it could be stable in bicarbonate electrolyte (pH 7.4 – 8.5 depending on CO_2 saturation). The introduction of 10 % vol. MIPA in methanol transferred the particles – from now on denoted as Cu-Ag (MIPA) - from hexane to the methanol phase, which suggests the adsorption of the ligand on their surface. The observed agglomeration at the bottom of the vial indicates a weaker stabilization by the shorter ligand. Next, the ligand removal was conducted by replacing the amine groups with sodium borohydride (BH_4^-, a hard base), which also acts as a reducing agent (BO_2^-/BH_4^- at –1.24 V vs. NHE [24]) that can prevent copper or silver oxidation. Particle coalescence evidenced that the ligand removal was effective and that the suspension was completely destabilized. This is similar to the Ag NPs (12 nm) of the same size recently studied by Buonsanti et. al.[12]. Ag NPs experienced self-sintering and formed 150 nm aggregates when the ligand exchange was attempted directly in solution. Therefore, the authors conducted ligand exchange on substrate-supported NPs. It is known that an extreme change of surface energy usually deteriorates the morphology and stoichiometry of the particles[25]. Because the surface state and atomic composition are critical parameters for CO_2 reduction, it is important to make sure that the former NP structure is preserved after the deposition onto the GDE. Hence, we first applied the same procedure using TEM grids in order to investigate particle immobilization on a substrate during the ligand treatment. Similarly, the same method was applied on GDEs prior to CO2R experiments, as will be discussed later on. Figure 2 shows the state of core-shell nanostructures after the ligand exchange and removal protocol on-substrate, investigated by means of high resolution HAADF-STEM. Cu-Ag (OAm) particles disclosed a homogeneous particle distribution with an equal spacing from each other (3.1 ± 0.4 nm) due to the length of the

tangled long alkyl chain – around 2.04 nm, which is the stretched size of the oleylamine[26]. The ligand exchange step causes the NPs to get closer to one another due to the shorter tail group of MIPA. EDX line scanning profile in Figure S4 (a – b) shows the strength of the Cu signal at the core of the particles, whereas the Ag signal had two peaks on both sides that correspond to the minima of the former. The elemental mapping in Figure S4 (d – f) also confirms the fact that the core-shell morphology of Cu-Ag particles was mostly preserved, with the exception of some particles that leached out.

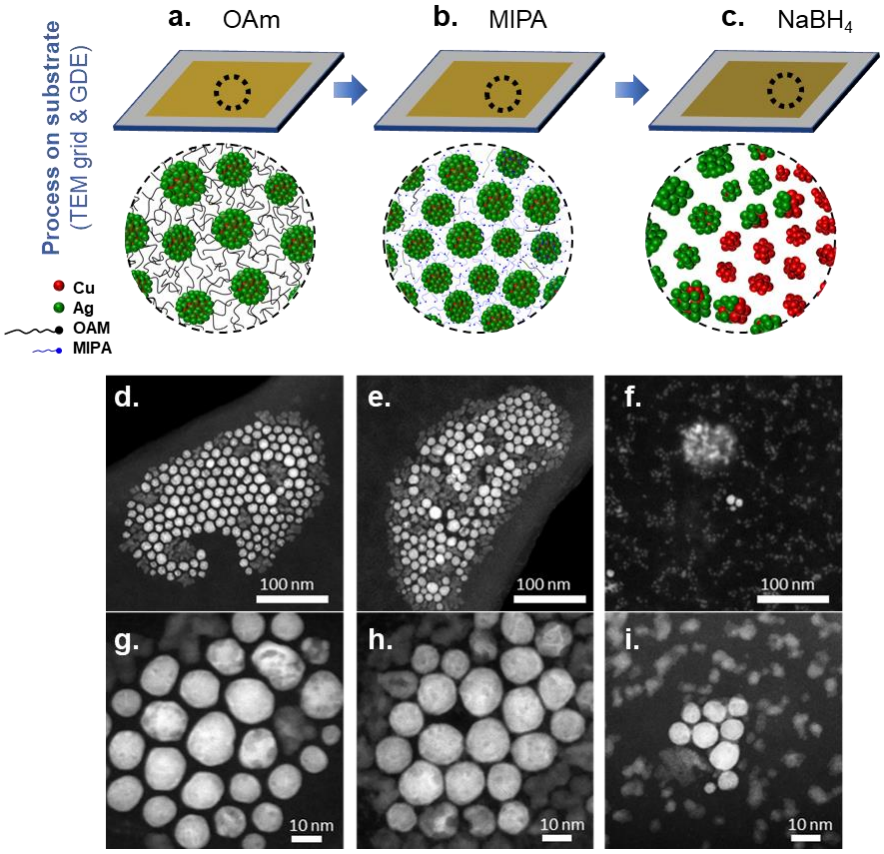

Figure 2. (a – c) The illustration of the ligand exchange and removal processes conducted on substrates of TEM grids and gas diffusion electrodes (GDEs) with deposited catalyst NPs. STEM images of Cu-Ag catalyst NPs on the TEM grid; **(d, g)** Cu-Ag (OAm), **(e, h)**

Cu-Ag (MIPA) and **(f, i)** Cu-Ag ($NaBH_4$).

Figure 2 (f – i) shows small ~5 nm aggregates found to be copper due to the rise of the copper signal in their EDX spectra in Figure S4 (c). These particles were not very stable, neither under the electron beam nor on the substrate. Lastly, the ligand removal of Cu-Ag core-shells was conducted using BH_4^- anion (denoted as Cu-Ag ($NaBH_4$)). We found segregated Cu and Ag particles accompanied by several stable Cu-Ag core-shell particles shown in Figure 2 (f – i) and Figure S5. It is certain that Ag particles suffered from self-sintering and agglomerated, as reported previously[12], whereas Cu particles were dispersed into nanoclusters throughout the substrate, a phenomenon known as fragmentation[27]. The *process on substrate* method was conducted on GDEs after the air-brushing of the catalyst-ink. The digital pictures of the electrodes taken at each step are given in Figure S6. Additionally, we observed 5 and 21 % of weight change of the catalyst loading after ligand exchange and removal, respectively – summarized in Table S1.

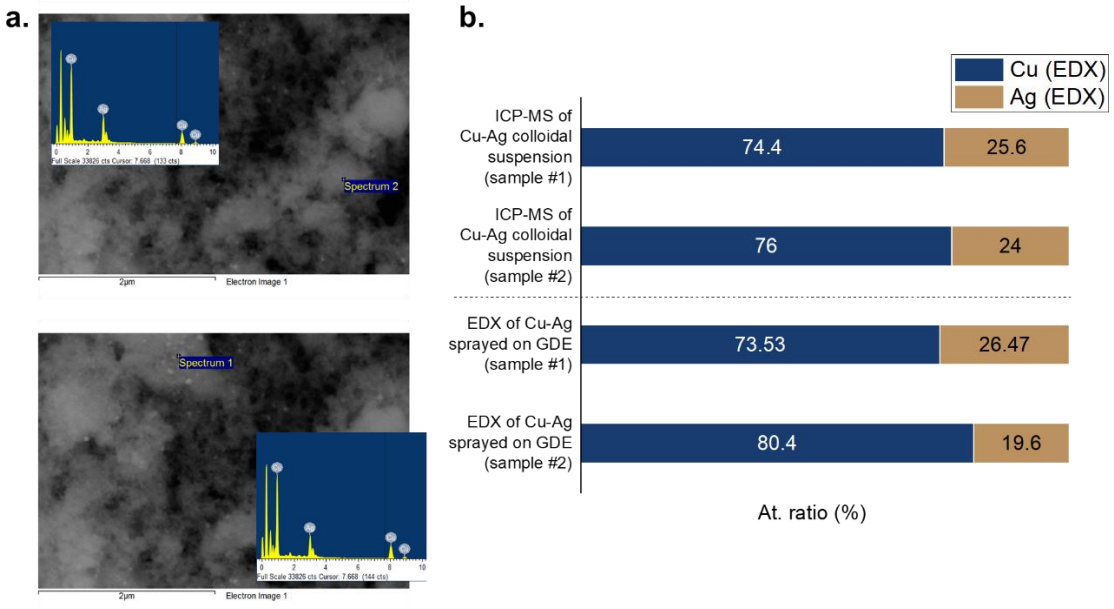

Figure 3. (a) SEM image of the Cu-Ag (OAm) nanoparticles which were air-brushed on

the gas diffusion electrodes (GDE). The spectrum at the insets show their EDX analysis. **(b)** The results of atomic ratio obtained by ICP-MS analysis of the Cu-Ag (OAm) colloidal solution and EDX analysis of the Cu-Ag (OAm) catalyst particles recovered from GDE.

We did not observe any color change in the solutions used for the ligand treatments or any sign of precipitation during the immersion steps. This indicated a well-adherent catalyst film on the GDEs. It is likely that the weight changes originated from the loss/substitution of alkyl chains of the ligands that are released from the particle surface as previously reported[15]. Additionally, we conducted EDX-SEM analysis to understand whether the weight change would be a preferential metal dissolution or not, as shown in **Figure 6**Figure 3(a). The elemental analysis of the catalyst film layer for Cu:Ag atomic ratio was found to agree well with that of the synthesis (4:1). Hence, the weight changes cannot originate from a specific metal dissolution during the immersion step. On top of that, ICP-MS analysis confirmed the same stoichiometry between the colloidal suspension and the sprayed ink given in Figure 3(b).

For a further confirmation of the ligand exchange and removal, we have checked the surface groups on the catalyst film coated electrodes by using infrared spectroscopy (IR) analysis. The high surface sensitivity of the attenuated total reflection (ATR-IR) mode enabled us to conduct a non-destructive examination of the Cu-Ag catalyst film on GDE surface prior to the CO2R reaction tests. The spectrum, shown in Figure 4a, reveals the characteristic peaks of the oleylamine (OAm) and isopropylamine (MIPA) groups. The three peaks at 2848, 2910 and 2945 cm^{-1} represent the C–H stretching modes of the oleylamine carbon chain[28], while the strong peak at 1458 cm^{-1} is associated with the C–H bending mode. These peaks are clearly visible at the spectra of Cu-Ag (OAm) which verify the capping of the oleylamine ligand.

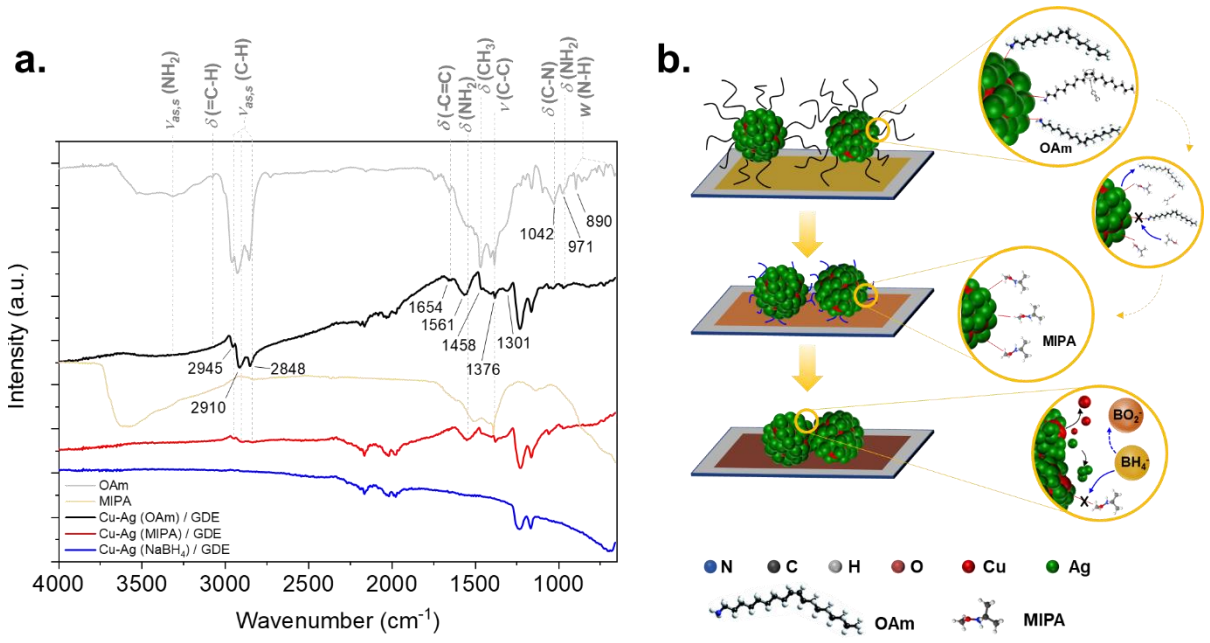

Figure 4. (a) ATR-IR spectra of oleylamine (OAm), isopropylamine (MIPA) and Cu-Ag catalyst coated gas diffusion electrodes **(b)** Schematic illustration of the mechanism of the ligand exchange and removal from the nanoparticles

Furthermore, the presence of various N–H peaks (NH_2 scissor mode at 1561 cm^{-1}, NH_2 bending at 971 cm^{-1}, and N−H wagging from 650 to 900 cm^{-1}) validate the amines that are bound to the surface of the Cu-Ag nanoparticles. On the other hand, C–N bond stretching at 1042 cm^{-1} and NH_2 stretching mode at 1561 cm^{-1} suggest the capping of the isopropylamine on Cu-Ag (MIPA) nanoparticles[29]. Additionally, the disappearance of the carbon double bond (C=C) specific to the long chain of the oleylamine ligand at 1654 cm^{-1} supports the ligand exchange from OAm to MIPA. Likewise, the missing of almost all of the characteristic peaks such as C−H vibration (~2900 cm^{-1}) and NH_2 vibrations (1561 cm^{-1}) support the removal of ligands as illustrated in Figure 4b. These findings are in good agreement with the recent work of

Dai et. al.[15] that studied similar Cu-Ag core-shell nanoparticles for application in conductive inks for printed electronics.

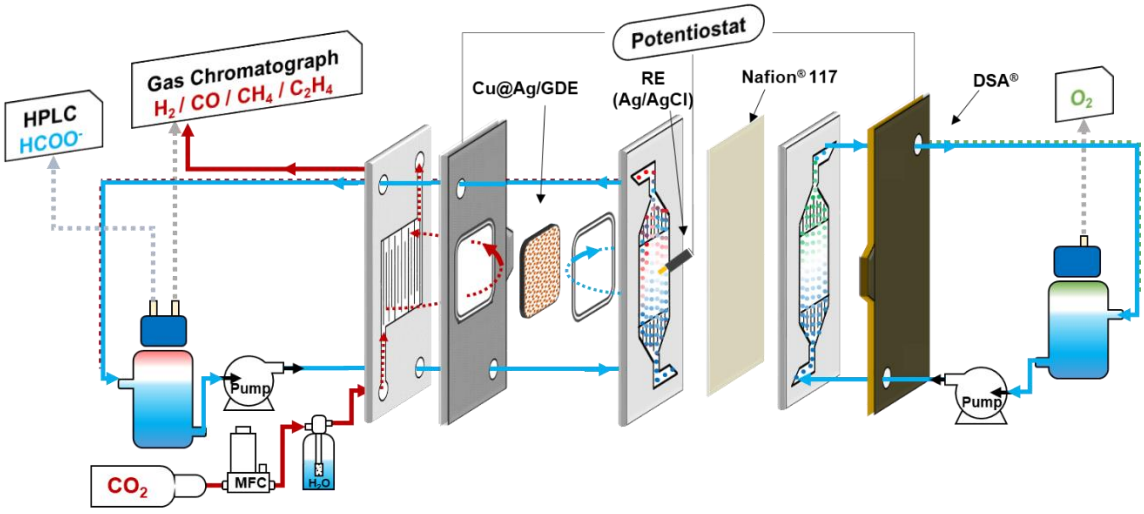

Figure 5. Schematic illustration of the stacked flow electrolyzer for CO_2 reduction experiments. Gas circulation was conducted in flow-by mode where both products (gas and liquid) were sampled from the catholyte container. The pre-humidified CO_2 gas (red arrows) and liquid electrolytes (blue arrows) were fixed to a flow rate of 40 and 20 ml/min, respectively. (MFC: mass-flow controller, RE: reference electrode, DSA®: dimensionally stable anode)

CO2R reaction experiments were conducted in an electrochemical flow-cell as illustrated in Figure 5. A gas-diffusion electrode was employed to eliminate any side effect of mass transport limitations (GDE). Cu@Ag catalysts were deposited onto the microporous layer made of a carbon and PTFE mixture to enable the gas diffusion while inhibiting the liquid flooding at the hydrophobic support. Further details for the sample preparation protocols are explained in the Experimental Section. In terms of the gas-feed method, the pre-humidified CO_2 gas was fed

through the back of the Cu-Ag/GDE catalyst-electrode assembly, of which the catalyst surface was facing an aqueous electrolyte of 0.5 M $KHCO_3$. As reported previously[30], higher salt concentration led to severe salt precipitation at the catalyst layer that create flooding canals over time, while lower concentrations gave rise to high cell voltages. On top of that, we have selected a cation-exchange membrane to minimize CO_2 crossover to the anode compartment in the form of carbonate and bicarbonate[31].

Cu-Ag (OAm), Cu-Ag (MIPA) and Cu-Ag ($NaBH_4$) on GDE electrodes were tested at potentials between −0.4 and −1.6 V vs. RHE. Figure 6 shows their faradaic efficiency (a – c) and partial current density (d – f), reflecting the effect of ligand exchange and removal on the activity and selectivity of the Cu-Ag catalyst nanoparticles obtained from the same synthesis. Formic acid (HCOOH) and carbon monoxide (CO) were the dominant products in the lower overpotential range (−0.4 to −1.1 V vs. RHE), and then followed by hydrocarbon products, such as ethylene (C_2H_4) and methane (CH_4), beyond −1.2 V vs. RHE, similar to the selectivity trends reported in the literature[32] with Cu-catalysts in a bicarbonate electrolyte (pH ~7.45). The highest faradaic efficiency of HCOOH was 28.5 % for Cu-Ag ($NaBH_4$) at -1.03 V vs. RHE (Figure 6a) and the partial current density was nearly two times higher than for the Cu-NPs (Figure 4b). At −1.1 V vs. RHE, the faradaic efficiency of CO for all the catalysts was higher than 60 %.

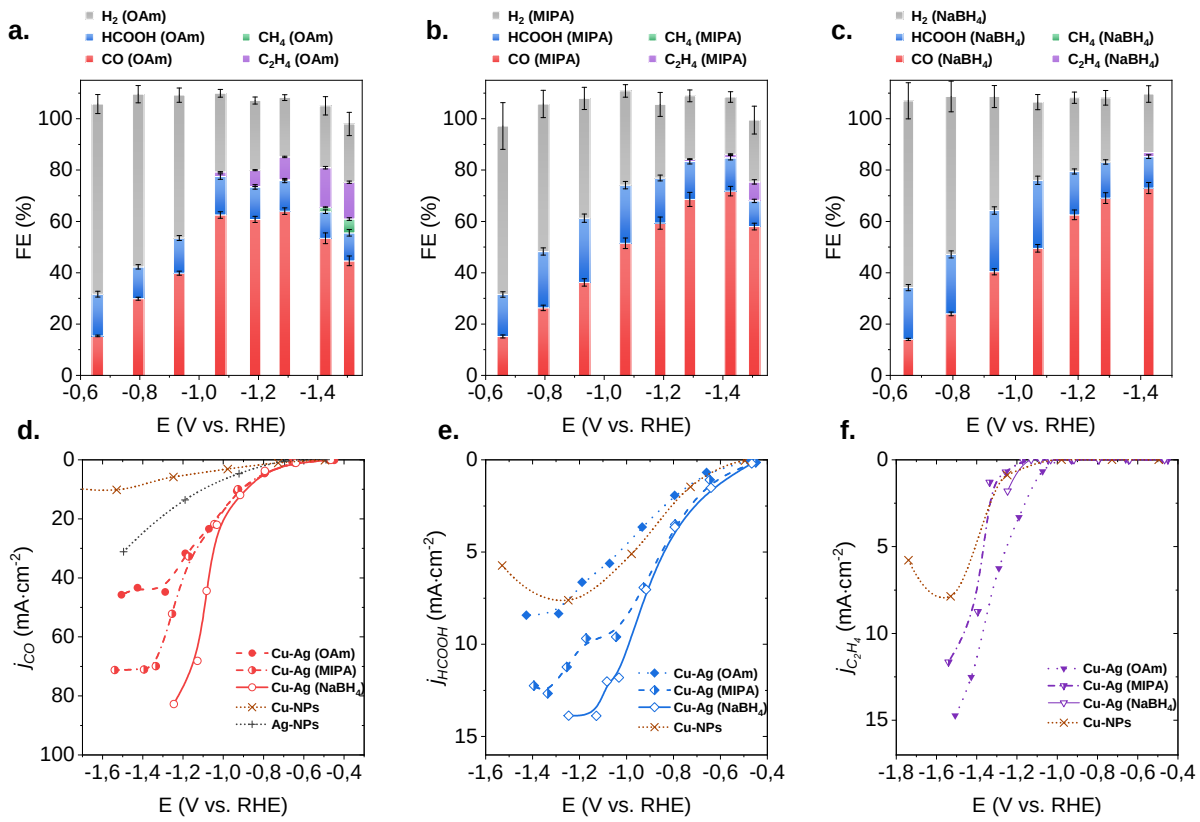

Figure 6. (a – c) The catalytic selectivity in terms of faradaic efficiency for Cu-Ag (OAm), Cu-Ag (MIPA) and Cu-Ag ($NaBH_4$), respectively; **(d – f)** the activity in terms of partial current density for HCOOH, CO and C_2H_4, respectively. Cu-Ag (OAm) as solid symbols, Cu-Ag (MIPA) as half-right symbols and Cu-Ag ($NaBH_4$) as open symbols are shown. The performance of Cu-NPs (cross symbols) and Ag-NPs (plus symbol) are also presented for comparison.

On the other hand, the exchange of the smaller group ligand (from OAm to MIPA) contributed to the partial current density of CO with an increment from 45.7 to 71.2 mA/cm^2, whereas its removal with reducing agent of $NaBH_4$ nearly doubled the initial value, reaching up to 82.7 mA/cm^2. This reflects the effect of the surface ligands on the electrical conductivity of nanoparticles, similar to the previous findings of Pankhurst et. al.[12]. Similarly, they observed an

increase of CO partial current density of Ag NPs as the tail length of the ligand was getting smaller. However, we obtained nearly one factor higher current density in comparison to their results, due to the use of GDEs in an electrochemical flow cell. This strategy noticeably improves the mass transfer of CO_2 and promotes a multitude of triple phase boundaries (TPBs), which are the meeting point for the electron, electrolyte and the reactant. This effect is even more prominent at higher current densities and potentials. At values between −1.1 and −1.6 V vs. RHE, Cu-Ag (OAm) particles exhibited the lowest voltage requirement for the production of C_2H_4. The catalyst capped with oleylamine ligand displayed 15.4 % selectivity at 0.5 M $KHCO_3$ electrolyte. The selectivity trend was similar to Cu-NPs, but the partial current density for ethylene was higher for the Cu-Ag (OAm) catalysts. It is possible that the active sites of Ag would act as an electron sink and promote CO spillover onto the Cu site for CO dimerization as shown previously with 25 nm Ag-Cu nanodimers[11]. Noticeably, the selectivity of CO vs. C_2H_4 for Cu-Ag ($NaBH_4$) catalyst was influenced by the rearrangement which could be more pronounced at different potentials (< −1 V vs. RHE) as previously shown in other studies[33]. Hence, it is possible that the ligand-free particles are more susceptible to relocate and aggregate compared to the ligand-capped particles under those operating conditions[34].

We sought therefore to develop a well-defined Cu-Ag catalyst layer for the comparison of their electrochemical surface properties. We prepared Cu-Ag catalyst-ink loaded glassy carbon electrodes (GCE) and followed the same *process on substrate* method for their surface ligand treatment. As shown in their light microscope images (Figure 7a), a smooth catalyst film was formed with Cu-Ag (OAm) on GCE indicating the homogenous distribution of the nanoparticles. After the ligand exchange and the removal steps, major changes in their film roughness were observed (See Supporting Info† at Figure S8 for the images at different magnification). Their

cyclic voltammetry measurements in CO_2 saturated electrolyte showed more than 2-fold change in the amount of the reduction current density at −0.7 V vs. RHE, after each treatment step presented in Figure 7b. We also note the oxidation stability of Cu-Ag (OAm) nanoparticles, once the electrode potential was swept to the positive direction of the OCV (Figure S9). In the same voltage window, Cu-Ag (MIPA) and Cu-Ag ($NaBH_4$) nanoparticles showed two oxidation peaks followed by two sharp reduction peaks. These are attributed to the copper redox reactions that usually occur at 0.34 and 0.52 V vs. SHE for $Cu^{0/2+}$ and $Cu^{0/+}$ under ideal conditions, respectively. It is unlikely that the oxidation peak would belong to silver (0.79 V vs. SHE for $Ag^{0/+}$) as it requires an extra 270 mV beyond the copper oxidation reaction. MIPA partially suppressed the oxidation reaction compared to Cu-Ag ($NaBH_4$) given the difference between the copper reduction peaks area, 0.21 and 0.38 mC, respectively. This highlights an advantage of the shorter ligand which can improve the current density by bringing the particles closer, yet prevent them to aggregate – shown in Figure S10. This would preserve the particle stability and could also facilitate the gas diffusion at the active sites.

Figure 7c shows the Nyquist plots of the EIS analysis conducted at −0.75 V vs. RHE in the CO_2 saturated electrolyte (See Supporting Info† at Figure S11 for the expanded view of the Nyquist and Bode plots for the potentials between −0.4 and −0.9 V vs. RHE). It is generally accepted that R_0 represents electrolyte ohmic resistance (R_s ~21 Ω). As the radius of semicircle is related to the charge transfer resistance, the decrease of semicircle diameters indicate the improvement of the electron transfer rate. This could be as a result of the larger interfacial contact area after ligand exchange and removal observed in HAADF-STEM images in Figure S10.

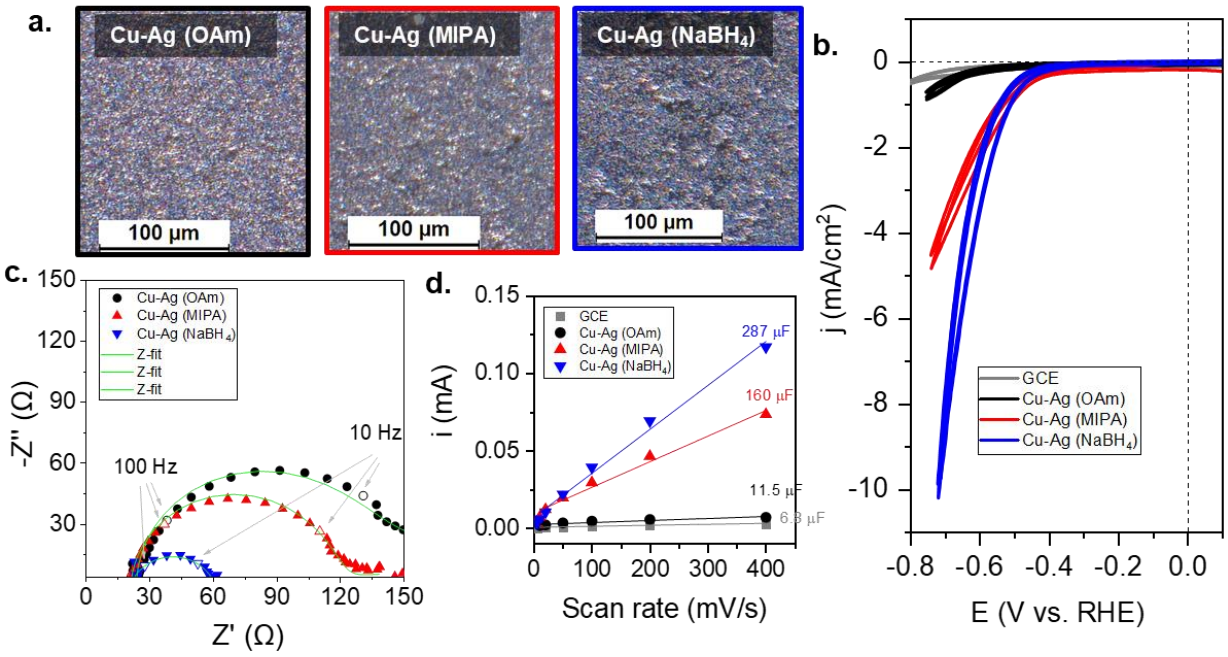

Figure 7. (a) Light microscope images of the Cu-Ag catalysts film on glassy carbon electrodes obtained before their testing; **(b)** cyclic voltammetry plots, **(c)** electrochemically active surface area analysis, and **(d)** EIS Nyquist plot conducted at -0.75 V vs. RHE in a CO_2 saturated 0.5 M $KHCO_3$ electrolyte for; Cu-Ag (OAm) catalyst on glassy carbon electrode (black line), after ligand exchange to Cu-Ag (MIPA) catalyst (red line) and ligand removal to Cu-Ag ($NaBH_4^-$) catalyst (blue line) in CO_2 saturated 0.5 M $KHCO_3$ electrolyte – the grey line is the signal of glassy carbon electrode as the blank.

Taking this into consideration, the fitting procedure can give an information about the processes involved in the reaction. The fitting-models based on their equivalent circuit and summary of their results are given in Figure S12 (a – d) and Table S2, respectively. The Bode plots revealed a single time constant related to the charge transfer between 1 and 100 Hz. An exception for Cu-Ag (OAm) electrode (Figure S11b) originated especially at lower potentials. The observation of multiple maxima shows that the data must be interpreted in terms of more

than one process. This could be related to the ligands acting as a blocking unit on the active parts, so they contribute to the total polarization resistance and create an equivalent capacitance value[35]. The charge transfer resistance (R_1) at the catalyst – solution interface was nearly 2-times higher for the oleylamine ligand than the isopropylamine ligand, 99.4 vs. 55 Ω respectively. The additional process was correlated with the contribution of the ligands to the total polarization resistance (R_2) which can occur at the ligand – solution interface, as illustrated in Figure S12 (e). On the other hand, Cu-Ag ($NaBH_4$) produced a smaller semicircle with 42 Ω resistance related to the charge transfer reaction, which was even lower than the NPs with the shorter ligand, Cu-Ag (MIPA). The electrochemically active surface area (ECSA) was measured using the current generated at the non-faradaic region of their CV plots shown in Figure 7d (and Supporting Info† at Figure S13 for the plots of their double-layer capacitance current versus scan rate). Their roughness factors (*RF*) were normalized against a mirror polished glassy carbon electrode, presented in Table S3. The results show that *RF* of Cu-Ag (OAm) catalyst (1.7) increased to the factor of 23 and 42 after the ligand exchange and removal, respectively. At this point, the improvement of the total current generation could be attributed to the increment of the surface area and the simultaneous decrease of the electrical resistance of the Cu-Ag catalyst electrodes. Moreover, the core-shell nanostructures are often used as conductive inks for their high electrical conductivity and oxidation resistance. The previous studies[14] measured a lower sheet resistance for the core-shell Cu-Ag nanoparticle films, along with the changes of their film thickness. The authors correlated this to the decrease of electrical resistivity by the formation of more compact particles after their ligand treatment.

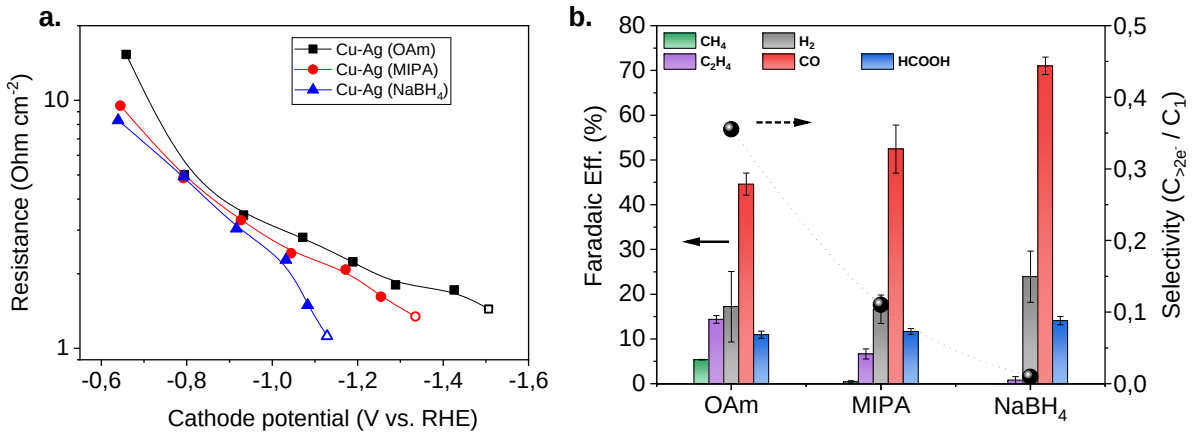

Figure 8. (a) Comparison of the overall cell resistance arise at different electrode potentials for the Cu-Ag catalyst electrodes. The points highlighted with the open symbols are equivalent to the test with cell current density of 100 mA/cm^2 and **(b)** Product distribution results of those highlighted points for Cu-Ag catalyst electrodes; in Faradaic efficiency (left y-axis) and C_{+2e}-/C_{2e}- selectivity (right y-axis).

Figure 8 (a) shows the resistance of the half-cell reaction measured from the individual electrode potentials during their CO_2 electroreduction tests. All the operational parameters were kept identical except for the catalyst type on the GDE substrate. The results display two distinct points; the first deviation starts at −1 V vs. RHE, whereas the second point of deviation is profound at −1.3 V vs. RHE. These points correspond to the electrical breakdown resistance of the surface ligands; monoisopropylamine and oleylamine, respectively. The catalyst layer resistance may impair the uniform charge distribution at higher current densities. For the larger GDE substrates (> 10 cm^2), this would lead to the potential differences along the electrode surface and affect the overall product selectivity. Figure 8 (b) displays the deviation in the product distribution after ligand exchange and removal. The faradaic efficiency for C_2H_4 production decreases from 14.3 to 6.6 % after the exchange to the smaller ligand group (OAm to

MIPA), whereas its removal gives rise to the formation of CO with 71 % faradaic efficiency for Cu-Ag ($NaBH_4$) catalyst electrode. Consequently, the C_{+2e^-}/C_{2e^-} product ratio decrease by half, from 0.42 to 0.23. This originates from the shift in the electrode potential by ~200 mV towards a positive direction after each treatment (-1.13V, -1.34V and -1.51 V vs. RHE, for Cu-Ag ($NaBH_4$) and Cu-Ag (MIPA) and Cu-Ag (OAm), respectively). These are in accordance with the results of EIS analysis that, the decreasing charge transfer resistance plays a significant role in the electrode performance.

For the electrochemical flow cells, the triple phase boundaries (TPB) are the active sites and the meeting point of the electron (by the catalyst electrode), the ion (through the electrolyte), and the CO_2 gas as the reactant. Thus, a limitation in the rate of the *electron transfer* would affect the TPB sites and the electrode performance as shown in Figure 8 (b). Accordingly, a change in the rate of the *CO_2 gas* would cause a similar effect on those active sites. In order to verify this, by maintaining the same current density (100 mA/cm^2), we have tested Cu-Ag (MIPA) under different CO_2 flow rates, fed to the electrochemical flow cell at 20, 40 and 80 mL/min (Figure S14). The product distribution shows a similar decreasing trend for C_{+2e^-}/C_{2e^-} ratio from 0.48 to 0.2. The minor increase in the C_2H_4 production (6.6 to 8 %) at 20 mL/min CO_2 flow remains to be investigated. However, the ethylene selectivity was proven to increase with the alkaline environment[36-37] so a lower amount of CO_2 concentration may cause the breakdown of the buffer and increase the local pH. On the other hand, at higher CO_2 gas flow rate (80 mL/min), the production of CO was promoted over H_2 evolution. The higher gas flow may promote CO formation by diminishing CO/CO_2 concentration[38] at the catalyst interface. This would impair the possibility for CO – CO coupling prior to the C_2H_4 formation as postulated earlier and may explain the diminishing of C_2H_4 production.

The comparison of CO2R performance amongst the different nanoparticles in the literature are given in Table S4. We selected the studies that performed colloidal synthesis using those similar ligands/capping agents to produce uniform core-shell particles. Additionally, Figure S15 illustrates the importance of the testing parameters for the true representation of the performance of those functional nanoparticles under industrially relevant conditions. Often upscaling would result in an inverse effect on the catalytic performance by impairing the reaction rate. Remarkably, the activity of Cu-Ag (MIPA) catalyst coated GDE electrode outperformed most of the core-shell bimetallic catalyst for CO partial current density, granting a tested geometric area of an order-of-magnitude compared to others in the list.

CONCLUSIONS

The ligand effect of nanoparticles on the CO_2 electroreduction performance was demonstrated with Cu-Ag core-shells (11.7 ± 2 nm) which was synthesized using colloidal methods. HAADF-TEM analysis showed that the particle size and shape was preserved after ligand exchange (OAm to MIPA), while the particle conformity was partially preserved with the subsequent ligand removal (using the $NaBH_4$ reducing agent). A process on substrate method was conducted to track these morphological changes on the catalytic performance for CO_2 conversion in an electrochemical flow cell. Compared to Cu-NPs, Cu-Ag (OAm) gave a lower on-set potential for the hydrocarbon production and a 2-fold higher partial current for ethylene. The ligand exchange (Cu−Ag (MIPA)) and removal (Cu−Ag ($NaBH_4$)) lowered the electrochemical charge transfer resistance and enhanced the overall electrochemically active surface area of the electrodes. This results in a total syngas production for Cu−Ag ($NaBH_4$) with 72.9 % CO and 23 % H_2 faradaic efficiency at total current density of ~113 mA/cm^2. The C_{+2e^-}/C_{2e^-} product ratio was in the order of Cu-Ag (OAm) > (MIPA) > ($NaBH_4$) which was associated to the decreasing overvoltage

requirement. EIS analysis showed a positive effect of the ligand exchange on the charge (electron) transfer whereas ECSA displayed an increase of the active sites that contributes to CO_2 mass transfer on the catalyst surface especially at higher current density. We correlate these findings to the increasing amount of the TPB sites (triple phase boundaries) after ligand exchange and removal, trivial for the flow-by gas circulation systems employing a large GDE substrate. Thus, the results and strategies disclosed here would be beneficial for the transfer of the well-defined nanoparticles onto the gas diffusion electrodes suitable to commercially relevant electrochemical CO_2 reduction conditions.

ASSOCIATED CONTENT

Supporting Information.

The following files are available free of charge on … at DOI ….

Details of the side effects from cell design and operating conditions, additional data on the HR-TEM for Cu NPs before the galvanic step, digital images for the *process on suspension* and *process on substrate* method, ICP-MS and EDX-SEM data, EDX-STEM data, Optical Microscope images of the glassy carbon electrodes, CV analysis, EIS Nquist and Bode plots, ECSA analysis and the data on the comparison to other core-shell catalysts in the literature for CO_2 electroreduction.

AUTHOR INFORMATION

Corresponding Author

* erdem.irtem@uantwerpen.be & tom.breugelmans@uantwerpen.be

Author Contributions

E.I. wrote the manuscript and carried out the materials synthesis, characterization and electrochemical evaluation. M.D. participated in the electrochemical analysis, D.A.E. conducted HR-TEM and provided help with the analysis of the results. D.C. assisted with the synthesis, scanning electron microscopy and spectroscopic analysis. S.L. and M.S.I. performed TEM and XRD analysis. S.B. and T.B. conceived and designed the project. All authors read and contributed to the manuscript.

The author would like to thank Olivier Voet from AXES Research Group, NANOlab Center of Excellence for the ATR FT-IR measurements and also acknowledge the assistance of Lien Pacquets and Dr. Thomas Altantzis from ELCAT, University of Antwerp for the electron microscopy analysis.

Funding Sources

The authors also acknowledge financial support from the university research fund (BOF-GOA-PS ID No. 33928). S. L has received funding from the European Union's Horizon 2020 research and innovation programme under the Marie Skłodowska-Curie Grant Agreement No. 665385.

REFERENCES

1. Birdja, Y. Y.; Pérez-Gallent, E.; Figueiredo, M. C.; Göttle, A. J.; Calle-Vallejo, F.; Koper, M. T. M., *Nat. Energy* **2019,** 4 (9), 732-745.
2. Burdyny, T.; Smith, W. A., *Energy Environ. Sci.* **2019,** 12 (5), 1442-1453.
3. Xie, H.; Chen, S.; Ma, F.; Liang, J.; Miao, Z.; Wang, T.; Wang, H.-L.; Huang, Y.; Li, Q., *ACS Appl. Mater. Interfaces* **2018,** 10 (43), 36996-37004.
4. Chang, Z.; Huo, S.; Zhang, W.; Fang, J.; Wang, H., *The Journal of Physical Chemistry C* **2017,** 121 (21), 11368-11379.
5. Wang, P.; Qiao, M.; Shao, Q.; Pi, Y.; Zhu, X.; Li, Y.; Huang, X., *Nat. Commun.* **2018,** 9 (1), 4933.
6. Ma, X.; Shen, Y.; Yao, S.; An, C.; Zhang, W.; Zhu, J.; Si, R.; Guo, C.; An, C., *J. Mater. Chem. A* **2020,** 8 (6), 3344-3350.
7. Sun, K.; Cheng, T.; Wu, L.; Hu, Y.; Zhou, J.; Maclennan, A.; Jiang, Z.; Gao, Y.; Goddard, W. A.; Wang, Z., *JACS* **2017,** 139 (44), 15608-15611.
8. Shao, Q.; Wang, P.; Liu, S.; Huang, X., *J. Mater. Chem. A* **2019,** 7 (36), 20478-20493.

9. Kim, D.; Xie, C.; Becknell, N.; Yu, Y.; Karamad, M.; Chan, K.; Crumlin, E. J.; Nørskov, J. K.; Yang, P., *JACS* **2017,** 139 (24), 8329-8336.
10. Buckley, A. K.; Lee, M.; Cheng, T.; Kazantsev, R. V.; Larson, D. M.; Goddard Iii, W. A.; Toste, F. D.; Toma, F. M., *JACS* **2019,** 141 (18), 7355-7364.
11. Huang, J.; Mensi, M.; Oveisi, E.; Mantella, V.; Buonsanti, R., *JACS* **2019,** 141 (6), 2490-2499.
12. Pankhurst, J. R.; Guntern, Y. T.; Mensi, M.; Buonsanti, R., *Chem. Sci.* **2019,** 10 (44), 10356-10365.
13. De Gregorio, G. L.; Burdyny, T.; Loiudice, A.; Iyengar, P.; Smith, W. A.; Buonsanti, R., *ACS Catal.* **2020,** 10 (9), 4854-4862.
14. Kim, N. R.; Lee, Y. J.; Lee, C.; Koo, J.; Lee, H. M., *Nanotechnology* **2016,** 27 (34), 345706.
15. Dai, X.; Xu, W.; Zhang, T.; Shi, H.; Wang, T., *Chemical Engineering Journal* **2019,** 364, 310-319.
16. Duarte, M.; De Mot, B.; Hereijgers, J.; Breugelmans, T., *ChemElectroChem* **2019,** 6 (22), 5596-5602.
17. Irtem, E.; Andreu, T.; Parra, A.; Hernández-Alonso, M. D.; García-Rodríguez, S.; Riesco-García, J. M.; Penelas-Pérez, G.; Morante, J. R., *J. Mater. Chem. A* **2016,** 4 (35), 13582-13588.
18. Chee, S.-S.; Lee, J.-H., *J. Mater. Chem. C* **2014,** 2 (27), 5372-5381.
19. Dai, X.; Xu, W.; Zhang, T.; Wang, T., *Industrial & Engineering Chemistry Research* **2018,** 57 (7), 2508-2516.
20. Muzikansky, A.; Nanikashvili, P.; Grinblat, J.; Zitoun, D., *The Journal of Physical Chemistry C* **2013,** 117 (6), 3093-3100.
21. Osowiecki, W. T.; Ye, X.; Satish, P.; Bustillo, K. C.; Clark, E. L.; Alivisatos, A. P., *JACS* **2018,** 140 (27), 8569-8577.
22. Rossi, L. M.; Fiorio, J. L.; Garcia, M. A. S.; Ferraz, C. P., *Dalton Trans.* **2018,** 47 (17), 5889-5915.
23. Ortega, S.; Ibáñez, M.; Liu, Y.; Zhang, Y.; Kovalenko, M. V.; Cadavid, D.; Cabot, A., *Chem. Soc. Rev.* **2017,** 46 (12), 3510-3528.
24. H. Cheng, K. Scott, K.V. Lovell, J.A. Horsfall, S.C. Waring, Evaluation of new ion exchange membranes for direct borohydride fuel cells, J. Membr. Sci. 288 (2007) 168–174.
25. Niu, Z.; Li, Y., *Chem. Mater.* **2014,** 26 (1), 72-83.
26. Mourdikoudis, S.; Liz-Marzán, L. M., *Chem. Mater.* **2013,** 25 (9), 1465-1476.
27. Popović, S.; Smiljanić, M.; Jovanovič, P.; Vavra, J.; Buonsanti, R.; Hodnik, N., *Angew. Chem. Int. Ed.* n/a (n/a).
28. Salavati-Niasari, M.; Fereshteh, Z.; Davar, F., *Polyhedron* **2009,** 28 (1), 126-130.
29. Ouellette, R. J.; Rawn, J. D. In *Organic Chemistry*, Ouellette, R. J., Rawn, J. D., Eds. Elsevier: Boston, 2014; pp 41-74.
30. De Mot, B.; Hereijgers, J.; Duarte, M.; Breugelmans, T., *Chemical Engineering Journal* **2019,** 378, 122224.
31. Ma, M.; Clark, E. L.; Therkildsen, K. T.; Dalsgaard, S.; Chorkendorff, I.; Seger, B., *Energy Environ. Sci.* **2020**.
32. Kuhl, K. P.; Cave, E. R.; Abram, D. N.; Jaramillo, T. F., *Energy Environ. Sci.* **2012,** 5 (5), 7050-7059.

33. Osowiecki, W. T.; Nussbaum, J. J.; Kamat, G. A.; Katsoukis, G.; Ledendecker, M.; Frei, H.; Bell, A. T.; Alivisatos, A. P., *ACS Appl. Energy Mater.* **2019,** 2 (11), 7744-7749.
34. Goodman, E. D.; Schwalbe, J. A.; Cargnello, M., *ACS Catal.* **2017,** 7 (10), 7156-7173.
35. Electrochemical Impedance Spectroscopy, Chapter 16, by Mark E. Orazem and Bernard Tribollet (2008) Wiley
36. Moura de Salles Pupo, M.; Kortlever, R., *ChemPhysChem* **2019,** 20 (22), 2926-2935.
37. König, M.; Vaes, J.; Klemm, E.; Pant, D., *iScience* **2019,** 19, 135-160.
38. Wang, X.; de Araújo, J. F.; Ju, W.; Bagger, A.; Schmies, H.; Kühl, S.; Rossmeisl, J.; Strasser, P., *Nat. Nanotechnol.* **2019,** 14 (11), 1063-1070.

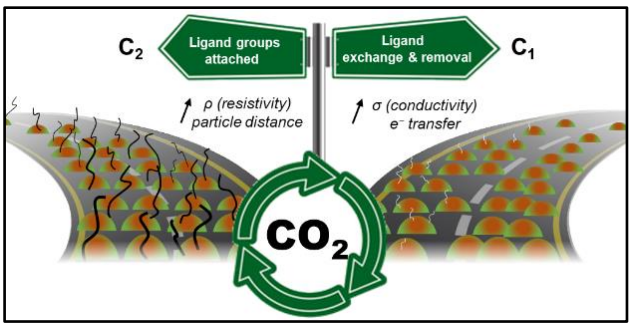
C2
Ligand groups attached
Ligand exchange & removal
C1
ρ (resistivity) particle distance
σ (conductivity) e⁻ transfer
CO2

T-o-C image